(Received 29 November 2024, Accepted 18 February 2025, Scheduled 27 February 2025)

Optimization Design for Bionic-Bamboo FPs of Coaxial Magnetic Gear Under Multi-Field Coupling

Yufeng Zhou[1,2], Heng Yang[1], Shuai Luo[2], and Xiuhong Hao[1,*]

[1]School of Mechanical Engineering, Yanshan University, Qinhuangdao 066004, China
[2]State Power Investment Corporation Research Institute, Beijing 102209, China

ABSTRACT: Coaxial magnetic gear (CMG) with magnetic field modulation mechanism features high torque density, non-contact transmission, and overload automatic protection, making it an optimal substitute for mechanical gears. Considering the unbalanced magnetic pull caused by the modulation effect of magnetic field and component eccentricities, the deformations of key ferromagnetic pole-pieces (FPs) are analyzed with and without magnetic-force-structure multi-field coupling. Then, the segmentation and reinforcement ideas based on bionic-bamboo are proposed in order to reduce the deformation of FPs. The functional relationships among FPs structural parameters, the output torque of CMG, and the deformation of FPs are established with the orthogonal test method and response surface method. Based on NSGA-III, the optimal parameters of FPs are obtained, and the corresponding deformation is greatly reduced. Finally, it is proved that the bionic-bamboo FPs can effectively reduce its deformation by the experiment and finite element simulation.

1. INTRODUCTION

Coaxial magnetic gears (CMGs) break through the topology of the traditional parallel axis magnetic gear and adopt the magnetic field modulation mechanism to realize the equal magnetic pole coupling of two rotors [1, 2]. CMGs have the advantages of high utilization rate of permanent magnets (PMs), larger output torque, and higher torque density, and can be widely used in vehicles, wind power, chemical industry, and other fields [3, 4].

As the actuator of the magnetic field modulation mechanism, the ferromagnetic pole-pieces (FPs) plays an important role in CMGs and is directly related to the output torque and transmission losses. Scholars have analyzed the influences of parameters such as the thickness [5], slot shape, and polar arc coefficient of FPs [6, 7] on the output torque. Output torques of CMGs have been enhanced by changing the structure and material of FPs. CMG with a double-layer FPs is introduced and increases the maximum torque by 40% [8]. To make full use of PMs leakage, a hybrid double-modulated magnetic gear with radial and transverse FPs is proposed, improves the torque density, and reduces the torque fluctuation [9]. Influences of material and stacking mode of FPs on the losses and efficiency are analyzed [10]. High-temperature superconducting materials instead of the silicon steel sheets have significantly relieved leakage flux, reduced losses, and improved transmission efficiency [11–14].

Combination of the skeleton made of non-magnetic engineering plastic and the silicon steel sheets is the main structural form of FPs. The plastic skeleton is obtained by mechanical processing. The poor binding power between engineering plastic and silicon steel sheets, and material properties of engineering plastics lead to low strength and stiffness of FPs, which affects the improvement of CMG output capacity. Scholars have adopted connection bridge [15] to improve the strength of FPs and minimize the reduction of output torque through structural optimizations. Meanwhile, an integrative injection molding structure of FPs is proposed and can effectively improve the carrying capacity [16].

CMGs with high torque density need a longer effective axial length. So, FPs is prone to transverse bending or swelling under the action of the unbalanced magnetic pull (UMP) and centrifugal force, which will result in the fatigue damage of FPs and rubbing against the outer rotor. Although some attempts have been carried out to improve the carrying capacity of FPs, the improvement of the radial structure are mainly the focus, and the deformations caused by axial bending has not been considered.

The study in this paper aims to improve the transmission capacity of CMGs by the design optimization of FPs. Considering the possible fixations of one end and two ends, the deformations of FPs under UMP and centrifugal force are analyzed based on the multi-field coupling of magnetic, force and structure fields. The segmented structure and stiffener based on bionic-bamboo are proposed, and the structure parameters of FPs are optimized based on NSGA-III algorithm. The effectiveness of the optimized structure is verified by experiment test, which provides theoretical and technical supports for the realization of the high torque density CMGs.

2. FPS STRUCTURE IN CMG

The CMG shown in Figure 1(a) consists of three basic elements: inner rotor, outer rotor, and FPs. FPs takes charge of modulating the magnetic fields and makes the main harmonics in two

* Corresponding author: Xiuhong Hao (hxhong@ysu.edu.cn).

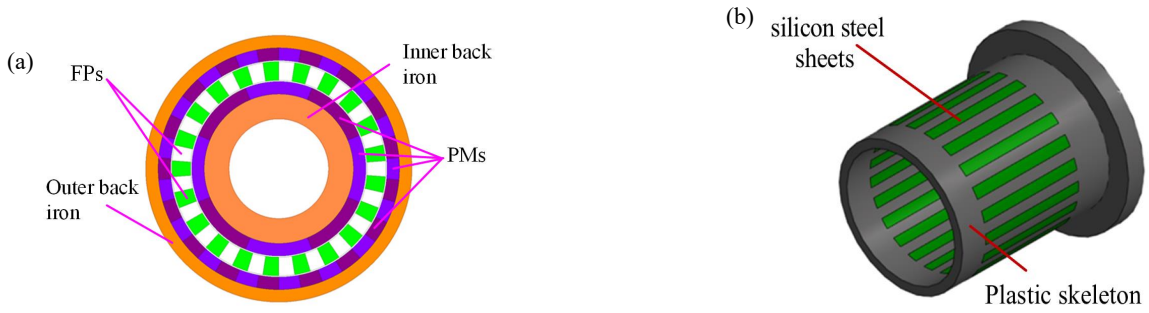

FIGURE 1. Structure diagrams of CMG and FPs. (a) Structure diagram of CMG. (b) 3D schematic diagram of FPs.

air-gaps beside it be consistent with the pole numbers of PMs on the corresponding rotor. Then, equal magnetic pole coupling can be achieved so as to transfer motion and power.

As the key component of CMG, FPs is arranged into a ring by the separation of magnetic and non-magnetic materials, as shown in Figure 1(b). The magnetic conductive material is generally made of stacked silicon steel sheets with excellent performances and amorphous alloy when CMGs run at the ultra-high speed. Engineering plastics are generally adopted to make the non-conductive parts.

Figure 1(b) shows that FPs has a hollow cup-shaped structure, and the skeleton is a squirrel cage structure with low stiffness and strength. FPs is subjected to large radial UMP during running and also suffers from centrifugal force when it is used as an output component. These make FPs prone to transverse bending or swelling and will be most likely to fatigue and creep. In a few cases, the rub will happen between FPs and PMs on the outer rotor. This will cause the damage of PMs and deteriorate the output performances of CMG.

3. DEFORMATION OF FPS UNDER UMP AND CENTRIFUGAL FORCE

Because of magnetic field modulation mechanism, the magnetic fields in two air-gaps are not evenly and symmetrically distributed, and FPs is subjected to UMP. Meanwhile, the special concentric structures of the three components in CMGs are also easy to cause the eccentricity and then aggravate the influence of UMP.

The parametric 3D model of CMG as shown in Table 1 is established. PMs on the inner and outer rotors are made of Nd-FeB and are radially magnetized. The magnetic block of FPs and the back irons of the inner and outer rotors are composed of silicon steel sheets, 35TW250. The non-magnetic part of FPs is made of epoxy resin by the injection molding.

To calculate the radial UMP on FPs, it is necessary to firstly calculate the magnetic force on the magnetic block in the x and y directions, as shown in Figure 2. Then, the corresponding coordinate system transformation and vector summation processing need be carried out, and UMP F_r on FPs can be obtained as follows:

$$\theta = 2\pi/42/2 + 2(n-1)\pi/21 \quad (1)$$

$$F_r = -F_x \sin\theta + F_y \cos\theta \quad (2)$$

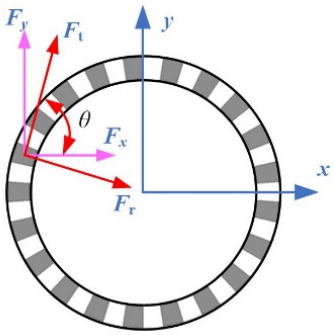

FIGURE 2. Schematic diagram of force analysis on FPs.

where θ is the angle between F_t and F_x; n is the number of magnetic conductive blocks; F_x, F_y, F_r, and F_t are the magnetic force components of FPs in x, y, radial, and tangential directions, respectively.

Eccentricities in CMGs include static eccentricity, dynamic eccentricity, and mixed eccentricity. When FPs is used as the output component, the worst conditions are the mixed eccentricity.

Thicknesses of the inner and outer air-gaps are selected to be 1 mm considering the larger output capacity of CMG and easier installation. Because of errors in component processing and installation, the mixed eccentricity is generally not more than 0.4 mm. When the static and dynamic eccentricity occurs, the initial eccentricity direction is in the positive direction of x axis, and UMP on FPs is shown in Figure 3.

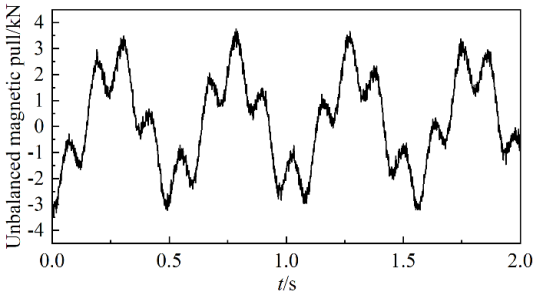

FIGURE 3. Radial UMP on FPs when there is mixed eccentricity.

Figure 3 indicates that UMP on FPs is relatively larger in value and varies with the obvious periodicity. These are related to the magnetic block arrangement and modulation effects of the magnetic field by FPs in CMGs. The more the number of

TABLE 1. Parameters of the sample CMG.

Number of pole pairs of the inner PMs	4	Number of pole pairs of the outer PMs	7
Number of FPs	21	Inner diameter of the inner back iron (mm)	80
Thickness of the inner back iron (mm)	20	Thickness of FPs (mm)	15
Thickness of the inner PMs (mm)	10	Air-gap thickness of inner and outer air-gaps (mm)	1
Thickness of the outer PMs (mm)	10	Axial effective length (mm)	140
Remanence of PMs (T)	1.3	Thickness of the outer back iron (mm)	10
Coercive force of PMs (kA/m)		1160	

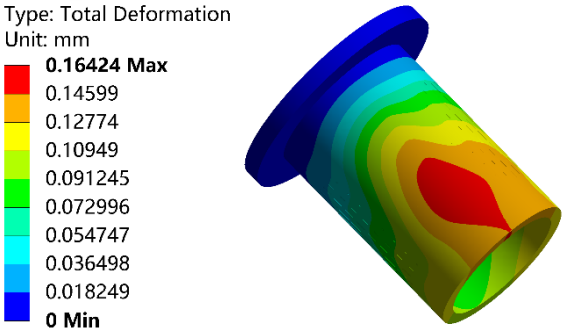

FIGURE 4. Deformation of FPs under UMP and centrifugal force.

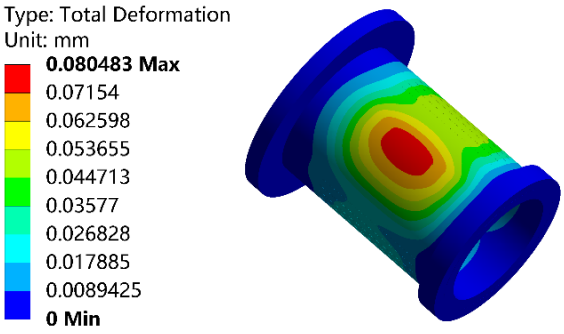

FIGURE 5. The deformation of FPs supported at both ends.

magnetic blocks in FPs increases, the faster the change period of UMP is, and the smaller the force on FPs should be.

When FPs outputs torque and movement, it will swell in the middle of the length by the centrifugal force. So, the influence of the centrifugal force should be considered too. When the input speed is 2000 r/min, the centrifugal force can be calculated by finite element simulation. The centrifugal force and radial UMP on FPs are introduced into the model built by Ansys Workbench, and the analysis results are shown in Figure 4.

Figure 4 shows that the cantilever end deformation of FPs is 0.16424 mm under the condition of one end support. In particular, serious radial and transverse deformations of FPs have occurred and will lead to size changes of the inner and outer air-gaps. The uneven air-gaps will further increase UMP and cause more serious deformations of FPs. The vicious cycle may cause the excessive deformation of FPs and lead to rub against with the outer rotor. So the coupling of magnetic, structure and force fields should be considered to calculate deformation of FPs more accurately.

In order to reduce the end deformation of FPs, a rolling bearing or annular sliding support can be added to the free end. The deformation of FPs is shown in Figure 5 under the mixed eccentricity and centrifugal force.

Figure 5 shows that the deformation of FPs supported at both ends is greatly reduced. The maximum deformation occurs in the middle of FPs and will increase when the rotational speed and dimensions in the radial and axial parameters increase.

Considering the multi-field coupling of magnetic, force and structure fields in CMG, the final deformation of FPs can be obtained by multiple iterations between electromagnetic module and the deformation module in Ansys Workbench [17]. The initial deformation of FPs is set to zero, and the corresponding UMP on FPs is imported into Ansys Workbench to analyze the deformation. Then, the deformation is considered to establish the new CMG model, and the latest UMP can be calculated. The calculation flowchart of FPs deformation under multi-field coupling model is shown in Figure 6. The stable deformation and deformation cloud image of FPs can be obtained after several cycles, as shown in Figure 7.

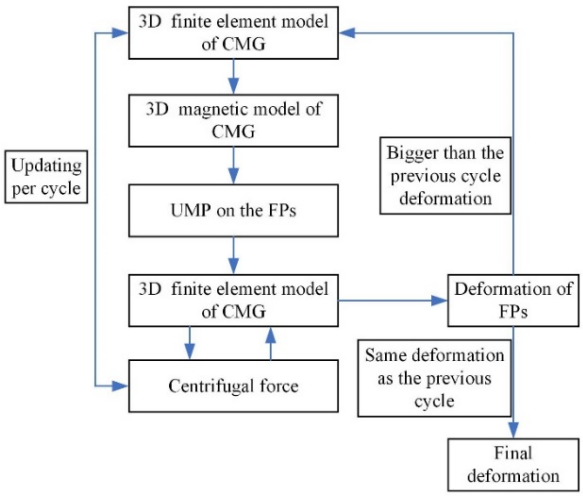

FIGURE 6. Flow chart of FPs deformation under multi-field coupling model.

When the coupling influence on the deformation of FPs, air-gaps thickness and UMP are considered, the deformation of FPs is much larger. That is, the deformation of FPs in a low power CMG exceeds 0.42 mm supported at one end and reaches 0.18 mm supported at both ends. The axial length of the higher

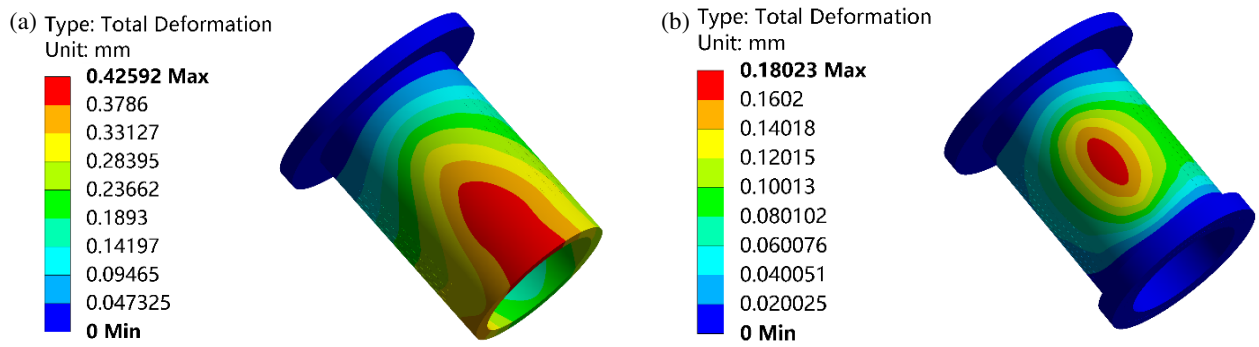

FIGURE 7. Deformation cloud image of FPs under multi-field cou-pling. (a) One end support. (b) Two end support.

power CMG is larger, and the axial strength and stiffness will be further weakened. If the air-gap is small, FPs will have greater radial deformation under the action of greater UMP and centrifugal force. These will make FPs fatigue or rub with the outer PMs.

4. DESIGN OPTIMIZATION OF FPS BASED ON BIONIC-BAMBOO AND NSGA-III

As a weak link, the bearing capacity of FPs must be improved to realize the high torque density CMGs. Considering the thin wall and squirrel cage structure of the supporting skeleton, the strength and stiffness of FPs can be increased by referring to the segmented bamboo structure. A rectangular structure of the stiffener can be selected, and the number of segments should be considered according to their influences on the output torque and deformation of FPs.

In this paper, orthogonal test and response surface method are adopted to confirm the variation rules of the output torque of CMG and FPs deformation with the segment of FPs, the width and thickness of the stiffener.

Orthogonal test method can reasonably determine the number of the simulation tests according to the number of factors, and the distribution of sample points follows the principle of uniformity. The information of the whole design space can be covered as much as possible, and the systematic error of calculation can be reduced. Enough data can be obtained by the reasonable experimental design in response surface method [18, 19]. The functional relationship between factors and response values can be fitted with the regression equation. Multi-variable and multi-objective problems will be solved by analyzing the regression equations with a specific algorithm to find the optimal parameters.

4.1. Orthogonal Experimental Design and Response Surface Method

The design factors that affect FPs deformation include the number of segments, the width and thickness of the stiffener. The variation ranges are shown in Table 2. If the number of segments is too large, the output torque of CMG will be reduced when its axial length is certain. When the output torque and FPs deformation are used as optimization objectives, the three-factor and three-level design table can be given, and the results are shown in Table 3.

TABLE 2. Optimize parameters and their value ranges.

Parameters	value ranges
Number of segments	$2 \sim 4$
Width of the stiffener (mm)	$1 \sim 9$
Thickness of the stiffener (mm)	$0 \sim 3$

4.2. Response Surface Analysis

In order to determine the relationships among the output torque, deformation, and design parameters of FPs, the following functional relationship is obtained by the polynomial fitting

$$\begin{aligned} T = {} & 784.71231 - 3.840801x_1 - 2.80210x_2 + 2.96145x_3 \\ & - 0.23576x_1x_2 - 0.11536x_1x_3 - 0.12786x_2x_3 \\ & + 0.46131x_1^2 + 0.19476x_2^2 - 0.76343x_3^2 \end{aligned} \tag{3}$$

$$\begin{aligned} u = {} & 0.1776 - 6.81\times10^{-3}x_1 + 1.37\times10^{-3}x_2 - 7.81\times10^{-3}x_3 \\ & - 7\times10^{-4}x_1x_2 - 1.45\times10^{-3}x_1x_3 + 7.7\times10^{-4}x_2x_3 \\ & + 1.57\times10^{-3}x_1^2 + 1.2\times10^{-4}x_2^2 - 1.4\times10^{-4}x_3^2 \end{aligned} \tag{4}$$

where T is the output torque; u is the deformation of FPs; x_1 is the number of FPs segments; x_2 is the width of the stiffener; x_3 is the thickness of the stiffener.

The correlation coefficients about the output torque and the deformation of FPs are 0.9813 and 0.907, respectively, which indicate that the response functions are well fitted and can well describe the change relationships between the changing factors and output response.

4.3. Structure Optimization of FPs Based on NSGA-III

4.3.1. Design Process of NSGA-III Algorithm

Maximum output torque of CMG and minimal deformation of FPs are selected as optimization objective to optimize FPs structure by NSGA-III algorithm. The constraint conditions are determined by the given ranges of the structural parameters, especially when the axial length of FPs is not changed. The specific flow of NSGA-III algorithm is shown in Figure 8.

TABLE 3. Orthogonal test table and simulation results.

No	Number of segments	width (mm)	Thickness (mm)	Outer torque (N · m)	deformation (mm)
1	2	1	2	778.6	0.179
2	2	3	2	772.8	0.176
3	2	5	1	767.3	0.175
4	2	7	3	765.5	0.172
5	2	9	3	762.1	0.170
6	3	1	3	773.4	0.179
7	3	3	0	768.6	0.174
8	3	5	2	765.3	0.174
9	3	7	0	763.2	0.174
10	3	9	1	762.8	0.166
11	4	1	1	775.2	0.179
12	4	3	3	767.4	0.175
13	4	5	0	762.3	0.175
14	4	7	2	759.9	0.170
15	4	9	0	758.6	0.177

As an efficient multi-objective evolutionary algorithm, NSGA II is widely used in industrial multi-objective optimization problems. When it comes to the high-dimensional optimization problems, the computational costs will increase exponentially [20, 21]. NSGA III was developed for the high-dimensional multi-objective optimization. In the process of individual selection of NSGA III, the method based on reference points is added and can effectively reduce the calculation costs [22, 23].

Step 1 Population initialization.

Considering the range of optimization parameters and population size in the multi-objective optimization of FPs, an initial population P_t with N individuals is randomly generated, and the fitness value of each individual is calculated. Then, the reference points evenly distributed in the target space are generated, and the number is H, $H = N$.

Step 2 Reproduction of offspring individuals for the next generation.

Crossover and mutation are performed to generate the next generation population Q_t, whose number is N. The newly generated population is combined with the initial population to form a new population of $2N$.

Step 3 Update of archive.

Fast non-dominated sort is carried out to the population R_t, and the individuals in the population are divided into different frontier layers, that is, $F_1, F_2, \ldots, F_i, \ldots, F_l$. When the number of layer individuals is greater than N, the individuals before the layer F_i will be added to the next generation population P_{t+1} according to the elite selection method. The niche preservation method based on reference points is adopted for the layer individuals F_i, and the excellent individuals are selected to join P_{t+1}.

Step 4 Check whether the termination condition is met.

Repeat Step 2–Step 3 until reaching the maximal iterations, and output the final Pareto optimal solutions.

Compared with NSGA-II, NSGA-III algorithm introduces reference points and selects individuals to promote the generation of solutions. The details are as follows [22, 23]:

(1) Structured reference point set.

In order to make the solution set obtained by the multi-objective optimization of FPs closer to the Pareto frontier and ensure that the reference points are uniformly covered in the entire optimized target space, the number of reference points is calculated by a systematic method, as shown in Equation (5):

$$\mathbf{H} = \begin{pmatrix} M+p-1 \\ p \end{pmatrix} \tag{5}$$

where M is the optimization target number; p is the average points for each optimization objective; H is the number of reference points, $H = N$.

(2) Adaptive normalization of the population individual.

The purpose of the adaptive normalization is to eliminate the dimensional and numerical differences between the objective function values in the multi-objective optimization of the bionic FPs. It is characterized by the introduction of extreme value points, as shown in Equation (6):

$$ASF(x, w) = \max_{i=1}^{M} \frac{f_i(x) - z_i^{\min}}{w_i}, \quad x \in S_t \tag{6}$$

where $f_i(x)$ is the value of x in the multi-objective optimization of FPs; $z_i^{\min}$ is the value of the ideal point in multi-objective optimization; w_i is the conversion weight.

Adaptive normalization is carried out on the value of each objective function fitted above with the intercept a_i of the hyperplane constructed by the extreme value points and

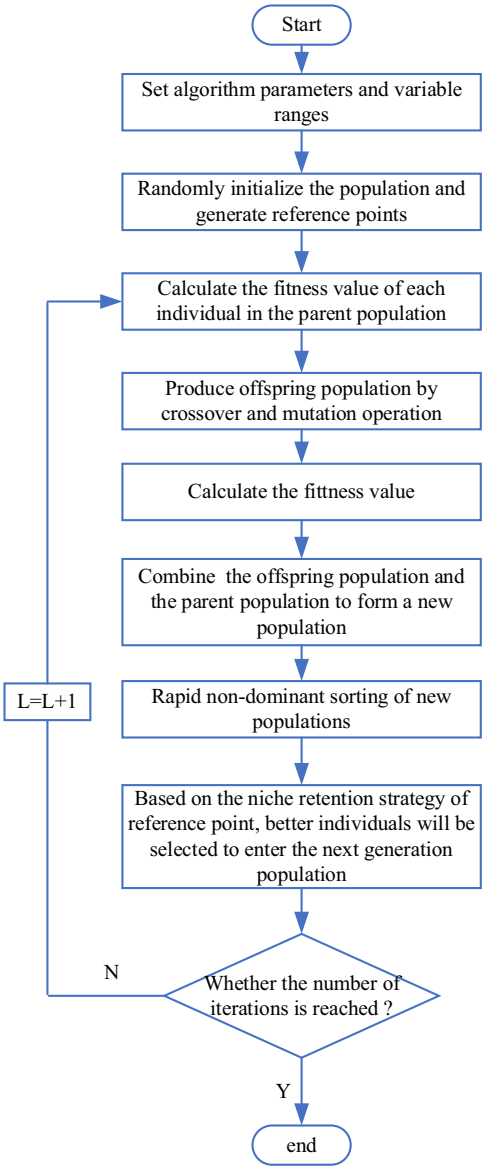

FIGURE 8. Flowchart of NSGA-III algorithm.

coordinate axis. After the adaptive normalization in multi-objective optimization, the value of x is shown in Equation (7):

$$f_i'(x) = \frac{f_i(x) - z_i^{\min}}{a_i - z_i^{\min}} \tag{7}$$

(3) Individual association operation.

Association operations are processes used to associate each individual in a population with the reference points to ensure the relative superiority of each individual in multi-objective optimization.

(4) Niche retention operation.

Firstly, the size of the niche is determined by the number of individuals associated with the reference points. The set of niches with the smallest habitat is identified, and the niches operation is conducted. For each selected niche, the following operations are performed: (a) If the minimum habitat is empty, the individuals with the shortest vertical distance from the reference line are selected from other niches to join the next generation population P_{t+1}; (b) If it is not empty, one is randomly selected to join the next generation population. The above operation is repeated until the number of the next generation population P_{t+1} reaches N.

4.4. Structure Optimization of FPs Based on NSGA-III

Before the multi-objective optimization of the bionic-bamboo structure of FPs, the relevant optimization parameter ranges and optimization conditions of the objective function should be set. The parameter optimization range is shown in Table 2. The optimization condition of the objective function is that the deformation of FPs is minimum when the output torque of CMG is larger.

$$\begin{cases} FindX\left(x_i\right) = (N, L, H) \\ x_i^L < x_i < x_i^U \end{cases} \tag{8}$$

where x_i^L and x_i^U are the upper and lower limits of each design dimension parameter, respectively.

$$\begin{cases} \max T = f_1\left(x_1, x_2, x_3\right) \\ \min u = f_2\left(x_1, x_2, x_3\right) \end{cases} \tag{9}$$

where T and u are the output torque and the deformation of FPs, respectively.

When NSGA-III algorithm is used to optimize FPs parameters, the initial population number was set to 150, the maximum number of iterations set to 300, the crossover probability set to 0.6, and the mutation probability set to 0.0001. A program written in Python is used to iteratively solve the objective function, and the problem of the maximum output torque is transformed into the minimum problem by the normalization operation. After the relevant parameters are set in the multi-objective optimization, FPs structure based on the bionic-bamboo is optimized according to the above the genetic algorithm optimization process. The Pareto optimal solutions finally obtained are shown in Figure 9.

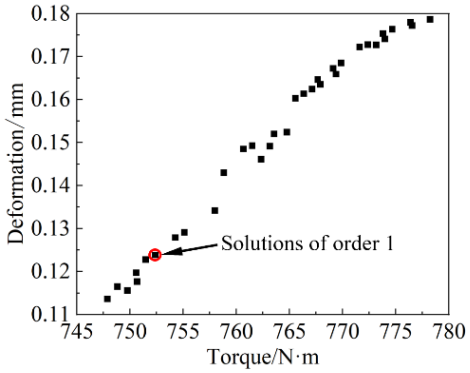

FIGURE 9. Pareto front obtained by NSGA-III.

In order to select the best combination from the 34 optimal solutions shown in Figure 9, technique for order preference by similarity to an ideal solution is adopted in this paper to evaluate

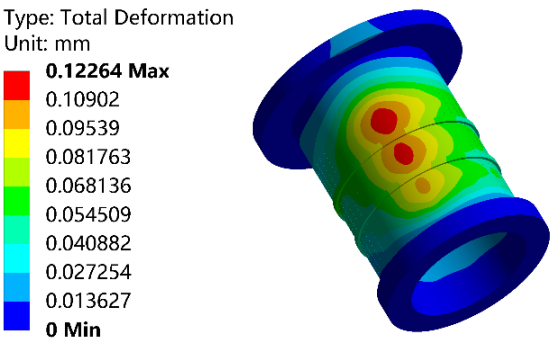

FIGURE 10. FPs deformation after the bamboo bionic optimization.

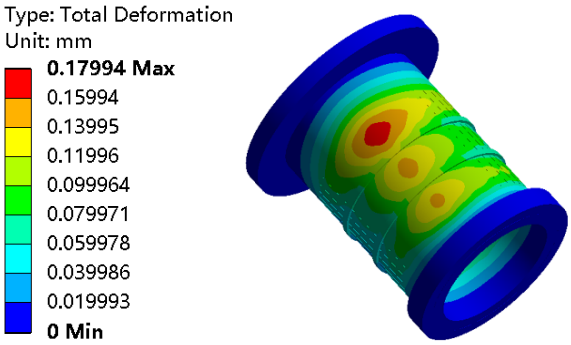

FIGURE 11. FPs deformation after the bamboo bionic optimization.

all solutions in the Pareto front. The weight ratio of the output torque and deformation of FPs is [0.45 0.55], and the optimal sorting solution is obtained as shown in Figure 9, whose corresponding parameters are 754.763 N · m and 0.1264 mm. That is, FPs is divided into 3 sections, and the width and thickness of stiffener are 7 mm and 3 mm, respectively.

Based on the obtained optimal results, 3D finite element model of CMG is established, and FPs deformation with the optimized structure can be obtained, as shown in Figure 10. To further verify the bearing capacity improvement of the bionic FPs, the maximum stress under the unbalanced magnetic pull and centrifugal force are calculated multiple times. In these calculations, the same reference prototype parameters and different speeds are selected. When the final deformation of the bionic FPs is basically equivalent to 0.18023 in Figure 7(b), the calculations end. The speed of the magnetic gear is 4400 RPM, and the corresponding stress cloud diagram of the bionic FPs is shown in Figure 11.

The output torque of CMG after the bionic-bamboo optimization of FPs has decreased from 786.439 N · m to 754.763, that is, the decline is 4.0%. However, Figure 10 shows that FPs deformation has been greatly reduced from 0.18023 mm to 0.12264 mm, namely, falling by roughly 31.95%. These can greatly improve the anti-deformation ability of FPs and effectively ensure the stable operation of CMG.

The centrifugal force of FPs increases with the increase of rotation speed in CMG. Figure 7(b) and Figure 11 show that the bionic FPs can withstand the higher rotation speed when the same deformation occurs.

5. DEFORMATION MEASUREMENT OF FPS AFTER BIONICBAMBOO OPTIMIZATION

In order to verify the anti-deformation ability of FPs after optimization, a deformation test platform has been built, shown in Figure 12. The sample of FPs is made strictly according to the simulation data [24]. As shown in Table 1, inner diameter and thickness of FPs are 116 mm and 15 mm, respectively. Length of the solid support part of two ends is 40 mm. The diameter of one side flange is 150 mm, and the corresponding thickness is 20 mm. The supporting skeleton of FPs is made of epoxy resin by the injection molding.

The deformation testing platform includes FPs sample, PTI dynamic tracking system, servo motor, centrifugal support fixture, and signal collector. Test points on FPs are selected, and the measuring marks are glued to the corresponding test sites. The signal generator and battery connected to the test points are fixed on FPs with sticky tape to prevent them from being thrown out due to centrifugal force. When motor runs and FPs is accelerated to 1000 r/min, and the deformations of the bionic FPs and conventional FPs are measured. Because FPs is not placed in CMG, it is mainly affected by the centrifugal force, and the deformation under UMP is not reflected.

Figure 13 and Table 4 show the maximum deformations of FPs under the centrifugal force before and after optimization.

When FPs runs at 1000 rpm, the deformations of the traditional FPs and bionic FPs are 0.04727 mm and 0.01968 mm, respectively. That is, FPs deformation is reduced by 58.4%, and the bionic FPs can effectively reduce its deformation.

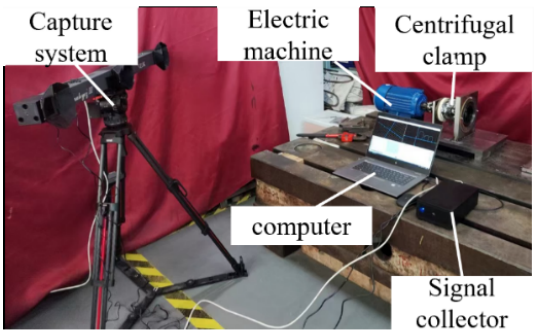

FIGURE 12. Deformation test platform of FPs.

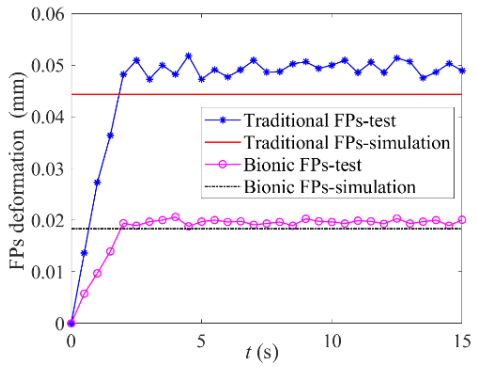

FIGURE 13. Deformation curves of FPs.

TABLE 4. The maximum deformations of FPs.

		Traditional FPs	Bionic FPs
Maximum deformations	Test	0.04727	0.01968
	Simulation	0.04435	0.01834

The deformation of the traditional FPs calculated by the finite element simulation is 0.04435 mm, and that of the bionic FPs is 0.01834 mm. The errors are 6.17% and 6.80%, respectively. These are caused by the deviation between the parameter setting of FPs and the actual material during the finite element modeling. Both the experiments and finite element simulation show that the strength and stiffness of FPs are greatly improved by the bionic reinforcement.

6. CONCLUSION

As a key component of CMG, FPs may deform greatly under the influence of UMP and centrifugal force. The bionic-bamboo FPs can provide theoretical and technical supports for the realization of the higher power density CMG.

(1) Under UMP and centrifugal force, FPs has more deformation when the multi-field coupling of the magnetic, force and structure fields is considered. These easily lead to the fatigue damage of FPs or rubbing between the FPs and outer rotor.

(2) An optimization method of FPs based on bionic-bamboo is proposed. Based on the orthogonal experiment and response surface method analysis, NSGA-III algorithm is adopted to obtain the optimal solution of Pareto, that is, optimal design. This can greatly reduce FPs deformation and improve the anti-deformation of FPs, which can effectively ensure the stable operation of CMG.

(3) The deformation measurement platform under centrifugal force is built for the optimized FPs. The result shows that the deformation of bionic FPs is 58.4% lower than that of traditional FPs.

ACKNOWLEDGEMENT

This work is supported by Hebei Natural Science Foundation (grant number: E2022203090), S&T Program of Hebei (grant number: 236Z1902G), and Science and Technology Project of the Hebei Education Department (grant number: ZD2022090).

REFERENCES

[1] Atallah, K. and D. Howe, "A novel high-performance magnetic gear," *IEEE Transactions on Magnetics*, Vol. 37, No. 4, 2844–2846, 2001.

[2] Rasmussen, P. O., T. O. Andersen, F. T. Jorgensen, and O. Nielsen, "Development of a high-performance magnetic gear," *IEEE Transactions on Industry Applications*, Vol. 41, No. 3, 764–770, 2005.

[3] Hou, S. B., S. Luo, J. Chan, W. C. Wu, Y. F. Zhou, and X. H. Hao, "Design formula of coaxial magnetic gear based on output torque," *Journal of Yanshan University*, Vol. 48, No. 4, 303–311, 2024.

[4] Wang, Y., M. Filippini, N. Bianchi, and P. Alotto, "A review on magnetic gears: Topologies, computational models, and design aspects," *IEEE Transactions on Industry Applications*, Vol. 55, No. 5, 4557–4566, 2019.

[5] Jing, L., L. Liu, Y. Zhang, and J. Su, "Parameters analysis and optimization design for concentric magnetic gear with halbach permanent-magnet arrays," *Electricmachines and Control*, Vol. 20, No. 3, 6–12, 2016.

[6] Kim, S. J., E.-J. Park, S.-Y. Jung, and Y.-J. Kim, "Transfer torque performance comparison in coaxial magnetic gears with different flux-modulator shapes," *IEEE Transactions on Magnetics*, Vol. 53, No. 6, 1–4, 2017.

[7] Liu, Y., J. Y. Cao, and J. C. Liu, "Mechanical performance analysis of field modulated magnetic gearbased on analytical model," *Journal of Mechanical Transmission*, Vol. 37, No. 1, 1–5, 2013.

[8] Zhang, X., X. Liu, and Z. Chen, "A novel dual-flux-modulator coaxial magnetic gear for high torque capability," *IEEE Transactions on Energy Conversion*, Vol. 33, No. 2, 682–691, 2017.

[9] Wang, J., C. Yu, B. Zhang, and R. Mo, "Electromagnetic performance analysis of a novel hybrid double-modulated magnetic gear with transverse skewed slotted magnetic field modulation ring," *Journal of Electrical Engineering & Technology*, Vol. 20, 403–414, 2025.

[10] Kowol, M., J. Kołodziej, M. Jagieła, and M. Łukaniszyn, "Impact of modulator designs and materials on efficiency and losses in radial passive magnetic gear," *IEEE Transactions on Energy Conversion*, Vol. 34, No. 1, 147–154, 2018.

[11] Cansiz, A. and E. Akyerden, "The use of high temperature superconductor bulk in a co-axial magnetic gear," *Cryogenics*, Vol. 98, 80–86, 2019.

[12] Jian, L., K. T. Chau, W. Li, and J. Li, "A novel coaxial magnetic gear using bulk HTS for industrial applications," *IEEE Transactions on Applied Superconductivity*, Vol. 20, No. 3, 981–984, 2010.

[13] Li, W., K. T. Chau, and J. Li, "Simulation of a tubular linear magnetic gear using HTS bulks for field modulation," *IEEE Transactions on Applied Superconductivity*, Vol. 21, No. 3, 1167–1170, 2010.

[14] Yin, X., Y. Fang, and P.-D. Pfister, "A novel single-PM-array magnetic gear with HTS bulks," *IEEE Transactions on Applied Superconductivity*, Vol. 27, No. 4, 1–5, 2017.

[15] Jian, L., Z. Deng, Y. Shi, J. Wei, and C. C. Chan, "The mechanism how coaxial magnetic gear transmits magnetic torques between its two rotors: Detailed analysis of torque distribution on modulating ring," *IEEE/ASME Transactions on Mechatronics*, Vol. 24, No. 2, 763–773, 2019.

[16] Lu, Y.-H., S. Luo, and S.-J. Wu, "Influence of material properties of magnetic adjusting ring on the loss of magnetic gear," *Journal of Mechanical Engineering*, Vol. 58, No. 22, 269–275, 2022.

[17] Hu, Y., T. Cao, and M. Xie, "Magnetic-structure coupling dynamic model of a ferromagnetic plate parallel moving in air-gap magnetic field," *Acta Mechanica Sinica*, Vol. 38, No. 10, 522084, 2022.

[18] Chen, W.-H., M. C. Uribe, E. E. Kwon, K.-Y. A. Lin, Y.-K. Park, L. Ding, and L. H. Saw, "A comprehensive review of thermoelectric generation optimization by statistical approach: Taguchi method, analysis of variance (ANOVA), and response surface methodology (RSM)," *Renewable and Sustainable Energy Reviews*, Vol. 169, 112917, 2022.

[19] Sun, Y., L. Cai, Y. Chen, and S. Wang, "Optimization of a high through-flow design turbine using response surface method,"

Physics of Fluids, Vol. 36, No. 4, 046106, 2024.

[20] Sun, X., N. Xu, and M. Yao, "Sequential subspace optimization design of a dual three-phase permanent magnet synchronous hub motor based on NSGA III," *IEEE Transactions on Transportation Electrification*, Vol. 9, No. 1, 622–630, 2023.

[21] Deb, K. and H. Jain, "An evolutionary many-objective optimization algorithm using reference-point-based nondominated sorting approach, part I: Solving problems with box constraints," *IEEE Transactions on Evolutionary Computation*, Vol. 18, No. 4, 577–601, 2014.

[22] Chen, C., Y. Yuan, and X. Yuan, "An improved NSGA-III algorithm for reservoir flood control operation," *Water Resources Management*, Vol. 31, 4469–4483, 2017.

[23] Wu, Y., D. Yan, J.-M. Yang, A.-P. Wang, and D. Feng, "Optimal scheduling strategy of electric vehicle based on improved NSGA-III algorithm," *Plos One*, Vol. 19, No. 5, e0298572, 2024.

[24] Holanda, J., "Analyzing the magnetic interactions in nanostructures that are candidates for applications in spintronics," *Journal of Physics D: Applied Physics*, Vol. 54, No. 24, 245004, 2021.